

Data-knowledge fusion driven frequency security assessment: A robust framework for renewable-dominated power grids

Author Information

Yurun Zhang¹, Wei Yao^{1*}, Yutian Lan¹, Hang Shuai¹, Shanyang Wei¹, Wei Gan², Chao Duan³, Jinyu Wen¹, Shijie Cheng¹

1 State Key Laboratory of Advanced Electromagnetic Technology, School of Electrical and Electronic Engineering, Huazhong University of Science and Technology, Wuhan, 430074, China.

2 School of Engineering, Cardiff University, Cardiff, CF24 3AA, United Kingdom.

3 School of Electrical Engineering, Xi'an Jiaotong University, Xi'an, 710049, China.

Abstract

Frequency security is critical for power grids, as deviations can trigger widespread outages and result in substantial economic losses. However, modern renewable-dominated power grids face an increased risk of insecurity due to low inertia and nonlinear frequency responses. To mitigate these risks, robust pre-fault frequency security assessment (FSA) is critical, which enables grid operators to implement preventive control strategies. To this end, we propose a data-knowledge fusion framework to achieve intelligent FSA in actual power grids. First, we classify FSA domain knowledge into two categories: (1) physics-guided knowledge directs the neural network pre-training process, ensuring that the fusion model's predictions consistent with frequency response mechanisms, and (2) physics-constrained knowledge establishes quantitative relationship on predictions, which forces them within theoretical ranges defined by domain knowledge. To integrate the two categories of domain knowledge, we develop a dual-channel neural network architecture to simultaneously capture both local and global characteristics related to power system frequency. Finally, we introduce a data-knowledge fusion training algorithm that integrates guided learning with constrained network architecture to enhance model robustness and generalization. Case studies on China's Yunnan Provincial Power Grid validate the superior performance of our framework: it reduces average prediction error to 1.26% (a 49.2% reduction over data-driven

methods), and maintains 97.60% accuracy in untrained scenarios (3.85% higher than data-driven methods), therefore satisfies the accuracy, robustness, and generalization requirements for actual power grids. The proposed methodology establishes a new paradigm for enhancing robustness of FSA in power grids, with potential application to cross-domain security assessment.

Introduction

Power systems are complex nonlinear networks that maintain stability through the real-time balance of generation and demand. Disruptions to the real-time balance between generation and demand can induce frequency deviations, which potentially results in severe frequency insecurity events. Frequency security denotes a power system's capability to regulate operational frequency within the prescribed limits during normal and contingency scenarios¹. However, the growing penetration of renewable energy sources has significantly changed frequency dynamics of bulk power systems, increasing the risk of frequency insecurity²⁻⁴. Recent large-scale blackouts - including the 2019 Great Britain outage (affecting over 1 million customers)⁵ and 2025 Iberian blackout (affecting 60 million customers with 1 billion economic losses)⁶ - highlight the growing criticality of frequency security in modern power systems^{7,8}.

Power system frequency security depends essentially on maintaining an instantaneous balance between power generation and demand. For individual generators, this balance involves mechanical and electromagnetic power (denoted as P_{mi} , P_{ei}), whereas system-wide it reflects the matching of total generation and load power (denoted as P_G , P_L). Under pre-fault steady-state conditions, generation precisely matches demand, which maintain near-constant system frequency. Following a fault, the grid enters a transient state where generation-load imbalance occurs, resulting in frequency deviation (denoted as Δf). The grid responds to frequency deviations through both inertial response (within approximately 0–10 seconds) and primary frequency control (within approximately 2–30 seconds)⁹, providing rapid frequency regulation. In conventional power systems, the inertial response (denoted as H)¹⁰ originates from synchronous generators, which converts the rotor's kinetic energy into electrical energy to mitigate power imbalances. Subsequently, the generator's governor activates primary frequency control, modulating output power proportionally to the frequency deviation through a droop characteristic (denoted as the regulation coefficient R) to restore the system frequency. However, modern power systems' frequency security faces dual challenges: (1) most renewable energy sources lack inherent inertial response due to the absence of rotors or limited stored kinetic energy in their rotors¹¹, and (2) the frequency regulation strategies of renewable sources are highly diverse and structurally distinct from those of droop based synchronous machines, complicating accurate frequency security assessment (FSA) in power systems with high renewable penetration¹²⁻¹⁵.

FSA represents a critical approach to mitigate frequency instability risks, which can provide an effective reference for operators to implement frequency control measures. FSA refers to using available system data to predict key frequency indicators, including maximum rate of change of frequency ($RoCoF_{max}$), frequency nadir (f_{nadir}), and quasi-steady-state frequency (f_{ss}), to evaluate post-fault frequency security. Based on the implementation timeline relative to contingency events, FSA frameworks can be classified into two categories: pre-fault FSA and post-fault FSA. Post-fault FSA utilizes time-synchronized measurements captured immediately following faults, incorporating both steady-state system conditions and fault characteristics to predict frequency stability^{16,17}. It enables rapid deployment of emergency frequency controls following contingency events. The post-fault FSA framework demands ultra-low-latency algorithms to prevent substantial economic losses from delayed emergency response¹⁸. The development of grid frequency active defense concept has shifted research focus toward pre-fault FSA, which evaluates all potential contingencies under current operational conditions using steady-state data and anticipate fault sets^{19,20}. Pre-fault FSA enables a dual defense strategy against frequency instability: (1) enhancing grid regulation capacity through optimized unit commitment for routine risks^{21,22}, and (2) implementing pre-configured emergency control schemes via decision tables for extreme contingencies²³. To enable proactive security defense prior to fault occurrence, this paper focuses on pre-fault FSA.

Methodologically, FSA approaches fall into two categories: knowledge-driven (KD) and data-driven (DD) paradigms, each exhibiting distinct advantages and limitations. The KD methods, including precise time-domain simulation (TDS) models and simplified aggregated system frequency response (ASFR) models, employ the power system mechanism for modeling, yielding high-credibility results. However, the inherent complexity of power systems hinders the simultaneous achievement of high accuracy (requiring precise models) and rapid speed (requiring simplified models) in FSA. For instance, precise TDS models require prohibitive computational costs (requiring tens of seconds per contingency for large-scale systems), making them impractical for bulk FSA applications²⁴⁻²⁷. However, simplified ASFR models, relying on idealized assumptions, introduce significant systematic errors in modern power system applications²⁸⁻³⁰. The DD methods employ data analytics, typically through deep learning models^{31,32}, whose exceptional nonlinear mapping capabilities could rapidly produce relatively precise results³³⁻³⁵. However, the inherent opacity of the DD models brings trust issues in terms of their predictions³⁶. These distrust manifest in two key aspects: (1) robustness - occasional large prediction errors may yield severely misleading guidance for system operators; and (2) generalizability - severe accuracy degradation when grid operational conditions significantly different from the training data. Recently, hybrid approaches are proposed to integrate the KD and DD methods, using their complementary strengths to enhance performance, with demonstrated success in several applications³⁷⁻³⁹. However, current hybrid approaches

remain limited to rigid knowledge integration, typically incorporating only model-based knowledge (simplified models such as ASFR) through simple concatenation. This inflexible fusion framework fails to resolve the aforementioned challenges due to inadequate knowledge representation and fusion techniques.

In this paper, we develop a novel data-knowledge fusion framework for pre-fault FSA to address critical robustness and generalization limitations in applying artificial intelligence (AI) techniques to real-world large-scale power grids. The main contributions of this work are as follows. First, we systematically classify FSA domain knowledge into two categories: physics-guided knowledge and physics-constrained knowledge. Physics-guided knowledge, which directs the neural network pre-training process, is represented as input-output equational mappings between steady-state data with anticipated faults and frequency security indicators. Physics-constrained knowledge, which establishes quantitative relationship on predictions, is formalized as equation/inequality output-output constraints linking frequency security indicators. To facilitate the deep integration of domain knowledge with DD models, we propose a dual-channel neural network architecture combining multilayer perceptrons (MLP) with graph convolutional networks (GCN) to simultaneously capture local and global topological features in steady-state data and anticipated faults. We introduce guided learning-constrained network (GL-CN) algorithms to effectively integrate both types of knowledge with DD models. Guided learning (GL) incorporates physics-guided knowledge into the training process, thereby enhancing model generalization capability while reducing sample requirements. The constrained network (CN) integrates physics-constrained knowledge into its graph neuronal connectivity, with a knowledge constraint loss function to force predictions within theoretical ranges defined by domain knowledge. Case studies on China's Yunnan Provincial Power Grid (3,734 nodes) demonstrate the proposed framework's superior performance and scalability for actual large-scale grid FSA applications: (1) Accuracy: achieves an average prediction error of 1.26%, representing a 49.2% reduction over DD methods; (2) Robustness: achieves <3% error using only 786 samples, outperforming DD methods by a 75% error reduction (data scarcity scenarios); tolerates 38.8% knowledge error while maintaining performance (knowledge imprecision scenarios); (3) Generalization: maintains 97.60% accuracy in untrained scenarios, outperforming DD methods by 3.85%. While the proposed framework has demonstrated superior performance in power system FSA, its methodological paradigm offers broader potential for AI deployment across engineering domains.

Results

2.1 Data-knowledge fusion framework for pre-fault FSA

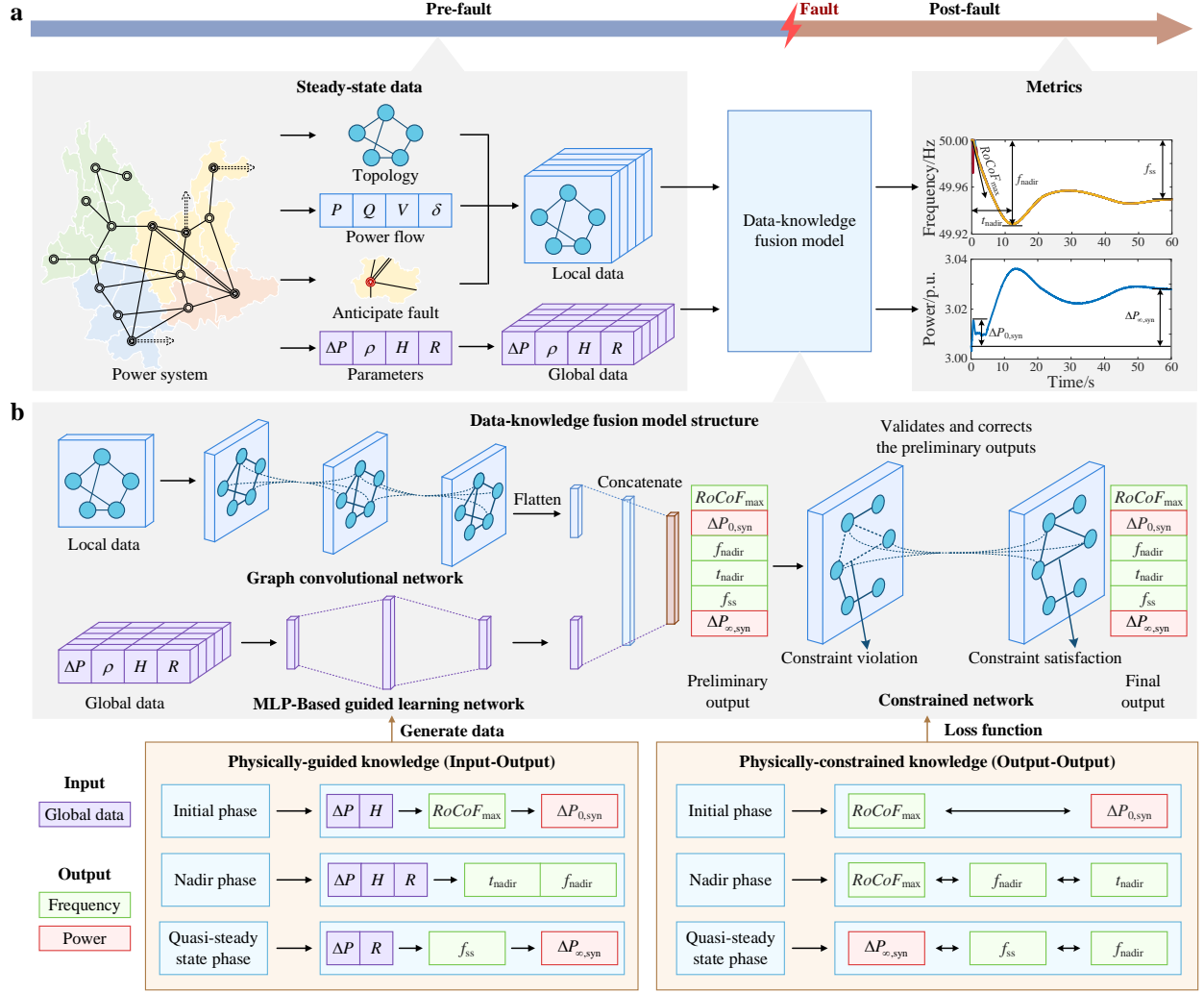


Fig. 1: The data-knowledge fusion framework for pre-fault FSA.

a Proposed flowchart for pre-fault FSA implementation. Under steady-state of the power system, three categories of operational data are obtained: (1) topology, (2) local data (power and voltage), and (3) global data (inertia level, regulation capacity, and renewable penetration). The anticipated fault set is embedded within this steady-state dataset. The data-knowledge fusion model outputs key dynamic responses following system fault, including: (1) frequency dynamics (maximum RoCoF ($RoCoF_{max}$), frequency nadir (f_{nadir}), time of frequency nadir (t_{nadir}), and quasi-steady-state frequency (f_{ss})) and (2) power dynamics (initial power transient ($\Delta P_{0,syn}$) and quasi-steady-state power adjustment ($\Delta P_{\infty,syn}$) of synchronous generators). **b** Architecture of the proposed data-knowledge fusion model. The GCN extracts topological and local data features, while the MLP processes global data features. These features are then flattened and concatenated to form high-dimensional spatial representations. A fully connected layer then generates preliminary results, which are subsequently calibrated by the CN to produce the final output.

Physics-guided knowledge is incorporated into the MLP-based guided learning network, while physics-constrained knowledge is integrated into the CN.

Our pre-fault FSA framework consists of three interconnected components: the power system (left), data-knowledge fusion model (center), and result outputs (right), as shown in Fig.1a. During steady-state operation, the system acquires real-time operational data (active/reactive power and voltage) from the supervisory control and data acquisition (SCADA) system at 30-second intervals, while assessing and retrieving critical system parameters (inertia and regulation coefficients) under current operational conditions. Simultaneously, the operator-defined set of anticipated faults is combined with steady-state operational data to create a hybrid dataset. The dataset is categorized into topological, local, and global data based on the system components they represent, with each data type subsequently processed by the trained data-knowledge fusion model. The model outputs characterize the system's frequency and power dynamics following the fault ($RoCoF_{max}$, f_{nadir} , t_{nadir} , f_{ss} , initial power transient ($\Delta P_{0,syn}$), quasi-steady-state power adjustment ($\Delta P_{\infty,syn}$)), with formal definitions of these metrics provided in Methods. We focus exclusively on synchronous machine dynamics to represent power dynamics, as their frequency-power relationships are both explicit and accurate. A system exceeds acceptable frequency security limits when any of the following thresholds are violated: $RoCoF_{max}$, f_{nadir} or f_{ss} . Such threshold violations indicate substantial frequency deviation and elevated risk of frequency insecurity.

To integrate power systems domain knowledge with deep learning models, we designed an architecture consisting of three core components: input channel, feature fusion module, and output channel, as shown in Fig.1b. For the input channel, topological and local measurements are transformed into graph-structured data for processing by the GCN channel, while global system parameters are routed to the MLP channel. The MLP channel is pre-trained based on GL to incorporate physics-guided knowledge to enhance its generalization. Following input processing, the features are projected into a high-dimensional space and undergo flatten and concatenation operations. These processed features are then transformed into preliminary predictions via a fully connected neural network layer. Finally, we implement a CN that both validates and corrects the preliminary outputs based on physics-constrained knowledge.

2.2 GL-CN algorithm for data-knowledge fusion

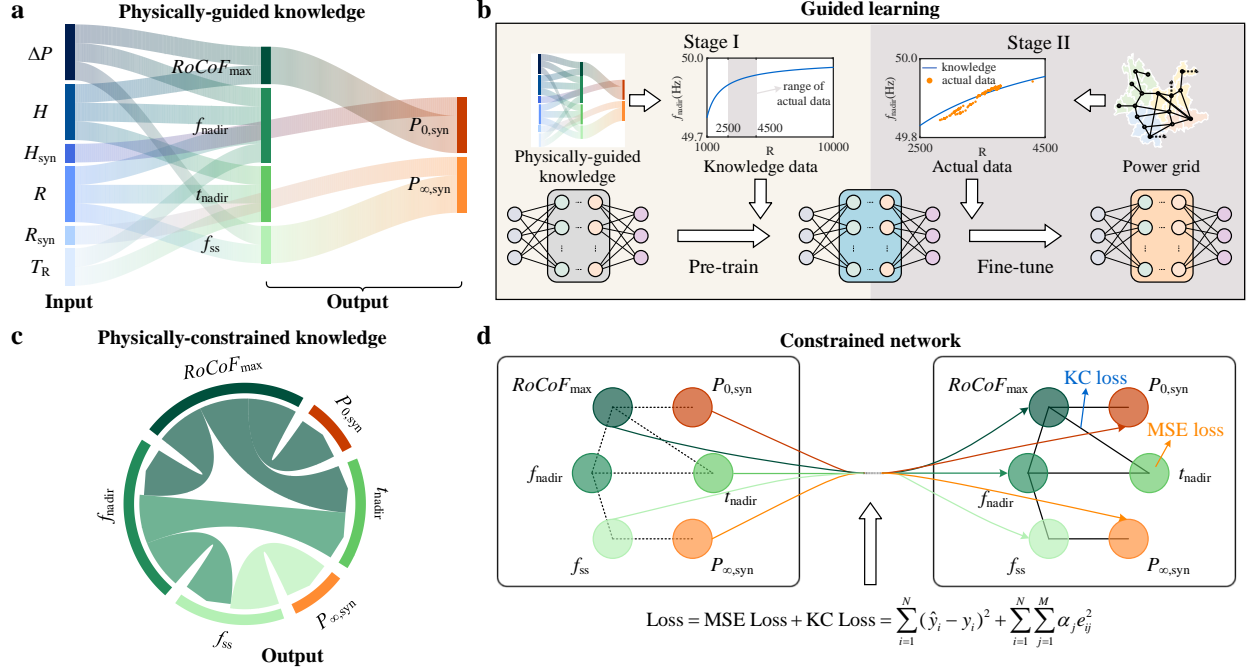


Fig. 2: The proposed GL-CN algorithm for the construction and training of data-knowledge fusion model.

a Schematic of physics-guided knowledge. The physics-guided knowledge characterizes the quantitative relationships between system parameters and system frequency stability indicators. System parameters include ΔP , H , inertia of synchronous generators (H_{syn}), R , regulation coefficient of synchronous generators (R_{syn}) and equivalent time constant of primary frequency modulation (T_R). System frequency stability indicators include frequency indicators ($RoCoF_{max}$, f_{nadir} , t_{nadir} , f_{ss}) and power indicators ($\Delta P_{0,syn}$, $\Delta P_{\infty,syn}$). **b** Flowchart of the proposed guided learning algorithm. The algorithm operates in two stages. In the pre-training stage (Stage I), it generates knowledge data using physics-guided knowledge encompassing broader parameter ranges than actual data, then uses these data for model pre-training. In the fine-tuning stage (Stage II), the model is optimized using actual data measured from the power grid. **c** Schematic of physics-constrained knowledge. The physics-constrained knowledge defines equality and inequality relationships among model predictions ($RoCoF_{max}$, f_{nadir} , t_{nadir} , f_{ss} , $\Delta P_{0,syn}$, $\Delta P_{\infty,syn}$), including post-fault frequency and power dynamics. **d** Flowchart of the proposed constrained network algorithm. The algorithm constructs a GCN incorporating physics-constrained knowledge, and employs combined mean squared error (MSE) and knowledge constraint (KC) loss functions for network training.

To ensure model generalizability across diverse operational conditions, we develop guided learning algorithms that integrate physics-guided knowledge into the DD framework. Fig.2a illustrates the schematic of physics-guided knowledge, derived from an aggregated simplified physical model of the power system. This representation captures the quantitative relationships between post-fault

frequency/power dynamics and system parameters, as formalized in Equation: $(RoCoF_{max}, f_{nadir}, f_{ss}, \Delta P_{0,syn}, \Delta P_{\infty,syn}) = \varphi(\Delta P, H, H_{syn}, R, R_{syn}, T_R)$. Details are described in Methods. As an aggregated representation, the physics-guided knowledge captures relationships between global data and output. We therefore embed the physics-guided knowledge within the global data input channel (MLP channel) of the proposed framework. Subsequently, the local data input channel (GCN channel) is trained using actual data. Fig. 2b illustrates the guided learning process, which comprises two principal stages. During pre-training, system parameters vary extensively beyond the existing sample set constraints to cover potential operational boundaries. For example, the pre-training expands the range of R values from the actual sample range of 2,500–4,500 to 1,000–10,000. During this stage, the model acquires physics-guided knowledge to enhance its generalization across diverse operational conditions. Simultaneously, by first training to achieve a level of accuracy comparable to KD methods, the model then requires significantly less actual data for its subsequent fine-tuning phase. During fine-tuning, we optimize the model with real power system data to account for power flow and topology factors that were not previously considered. The pseudo-code for the guided learning algorithm is detailed in the Supplementary Information.

The constrained network algorithms are developed to integrate physics-constrained knowledge, ensuring the robustness of the model output. Fig.2c visualizes the physics-constrained knowledge, derived from domain knowledge categorizing fault aftermath into three distinct periods: (1) fault inception, (2) frequency dip, and (3) frequency recovery, with corresponding frequency-power constraints for each period. The physics-constrained knowledge is mathematically represented as a unified data structure: $\psi(RoCoF_{max}, f_{nadir}, t_{nadir}, f_{ss}, \Delta P_{0,syn}, \Delta P_{\infty,syn} < \varepsilon)$, where ε denotes the permissible error threshold. Implementation details are provided in Methods. Fig.2d illustrates our constrained network algorithm, which implements connection relationships between nodes based on physics-constrained knowledge. Within the GCN, pairwise-connected nodes exchange information to enforce constraint relationships between outputs. The constrained network corrects output predictions by jointly optimizing both mean squared error (MSE) loss and knowledge constraint (KC) loss during training, which is detailed in the Supplementary Information. During prediction, the model validates initial outputs against the KC loss. Predictions satisfying the KC threshold are retained, while others are corrected by the constrained network. Following KC loss validation and constrained network correction, the model can achieve significantly enhanced the robustness of the output. The pseudo-code for the constrained network algorithm is also detailed in the Supplementary Information.

2.3 Model training and application in actual power systems

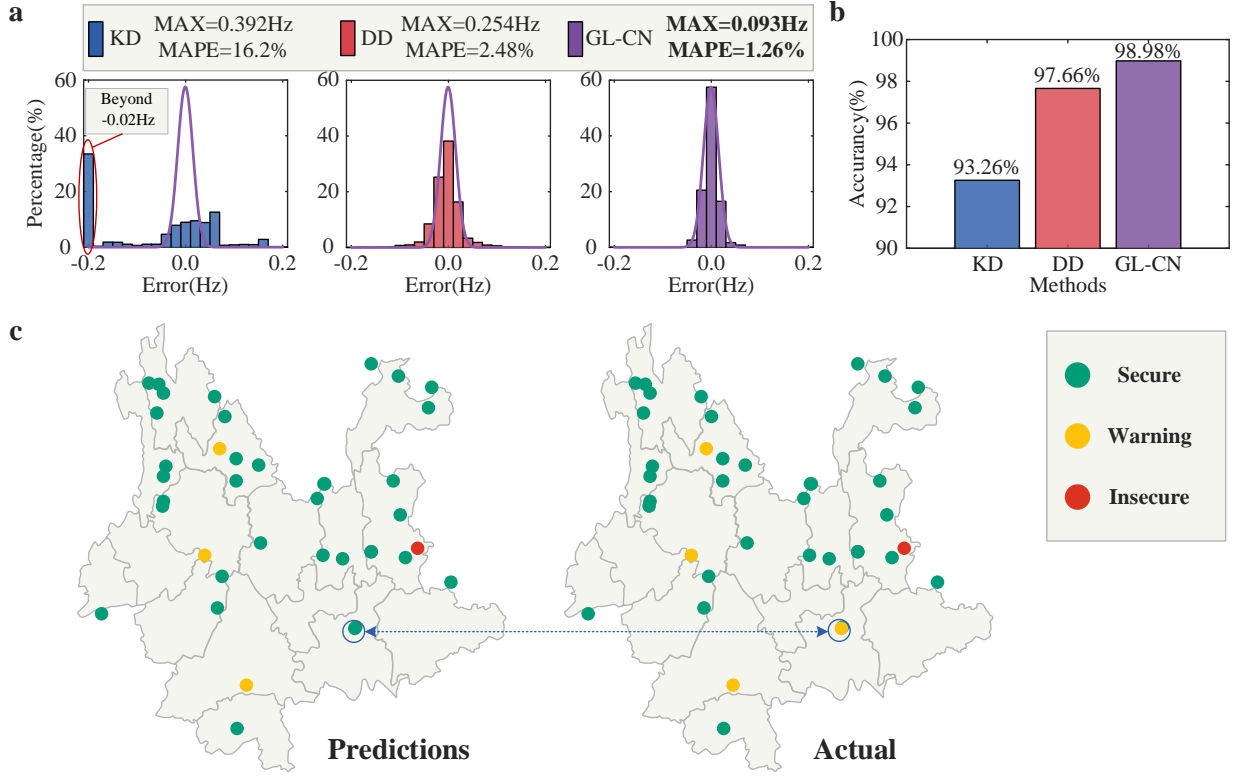


Fig. 3: Model performance in the Yunnan Provincial Power Grid.

a Distribution of prediction errors for the two benchmark methods (KD, DD) and proposed method. The histograms represent the distribution of errors between -0.02 and 0.02 Hz, and the curves represent the probability densities of the errors of the proposed GL-CN methods. **b** The accuracy of FSA predicted by two benchmark methods (KD, DD) and proposed method. **c** FSA results of proposed framework (left) and time-domain simulation (right) in winter operation mode of Yunnan Grid. Each data point corresponds to an anticipate fault, with color indicating the FSA output: red (insecure), yellow (warning), and green (secure).

We use China's Yunnan Provincial Power Grid as a practical test case to illustrate the performance of our framework. The Yunnan power grid, located in southwestern China, features abundant renewable energy generation (wind and photovoltaic) and multiple high voltage direct current (HVDC) transmission lines for power export. The network comprises 3,734 equivalent nodes, 794 power stations, and 4,350 alternating current (AC) lines serving 546 equivalent loads. With 46 GW of installed renewable capacity (32.4% of total generation capacity) and 31.2 GW of DC transmission capacity (47.1% of total power output), the system represents a high-penetration renewable grid with significant power export capabilities. Its high renewable penetration, low system inertia, and complex frequency dynamics, combined with its variable operational modes, introduce significant frequency security challenges, making it an ideal test case for validating the proposed method.

Using Yunnan power grid operational data, we generated a dataset comprising 12,707 samples (see Methods). The dataset comprises diverse steady-state operational conditions and anticipate fault scenarios. The steady-state conditions include five typical operation modes (40%-60% renewable energy penetration) generating 97 distinct current levels through operational adjustments. The fault scenarios comprise 131 common power imbalance events, including DC blockings, generator trippings, and load rejections. We selected 80 operational conditions (10,480 samples, 40%-55% renewable energy penetration) to create the standard dataset, which was randomly partitioned into training (70%), validation (15%), and test (15%) sets. The remaining 17 operational conditions (2,227 samples, 60% renewable energy penetration) were reserved exclusively for evaluating model generalization performance (Section 2.5).

As detailed in Section 2.2, model training proceeds through three phases. In the guided learning pre-training phase, we freeze all layer weights (learning rate = 0) except for the MLP layer, which trains exclusively on physics-guided synthetic data to learn fundamental physical principles. The second phase involves fine-tuning, where the entire network trains on real operational data to adapt to actual grid conditions. In the third phase, we train the constrained network using knowledge-based loss functions to enhance the physical robustness of the model. Pseudo-code and visualizations of all training phases are provided in Supplementary Information.

To validate the data-knowledge fusion effectiveness, we compared our GL-CN method against KD and DD approaches in both frequency prediction accuracy and FSA performance (see Methods for evaluation metrics). Fig.3a displays the prediction error distributions (-0.02 to 0.02 Hz) for all methods: KD, (left), DD, (center), and our GL-CN method (right). The outermost bars of each histogram represent the proportion of outliers beyond ± 0.02 Hz. We include the probability density distribution of our method's errors for comparative analysis. The figure reveals distinct error patterns: (1) KD exhibits the largest average error (uniform distribution, characteristic of systematic error); (2) DD shows spiked distributions (-0.02 to 0.02 Hz range) resembling random error; and (3) our GL-CN method demonstrates superior accuracy with tighter error bounds (± 0.01 Hz) and peaked distribution. Fig.3b compares the assessment accuracy of all three methods: while KD and DD achieve 93.26% and 97.66% accuracy respectively (see Supplementary Information for their risk distributions), our GL-CN method reaches 98.98% accuracy. In summary, our data-knowledge fusion approach enhances both prediction accuracy and reliability, offering power system operators robust decision-support.

Following training, we evaluated the model by: (1) predicting frequency responses for all anticipated faults under given operational conditions, and (2) classifying each outcome using predefined security thresholds (in Methods) into three categories: secure, warning, or insecure. All results for each operational condition are aggregated in Fig.3c to visualize frequency security risks, with complete datasets provided in Supplementary Information. Fig.3c display frequency security risks for the winter

operation mode, with (a) showing results from our data-knowledge fusion approach and (b) presenting time-domain simulation benchmarks for validation. Our method achieves comparable accuracy to time-domain simulations in assessing frequency security risks (Fig.3c), while offering substantial computational efficiency: 0.7 seconds per operational condition versus 1.5 hours for conventional simulation, enabling rapid power system FSA.

2.4 Evaluating data requirements and knowledge accuracy thresholds for the proposed method

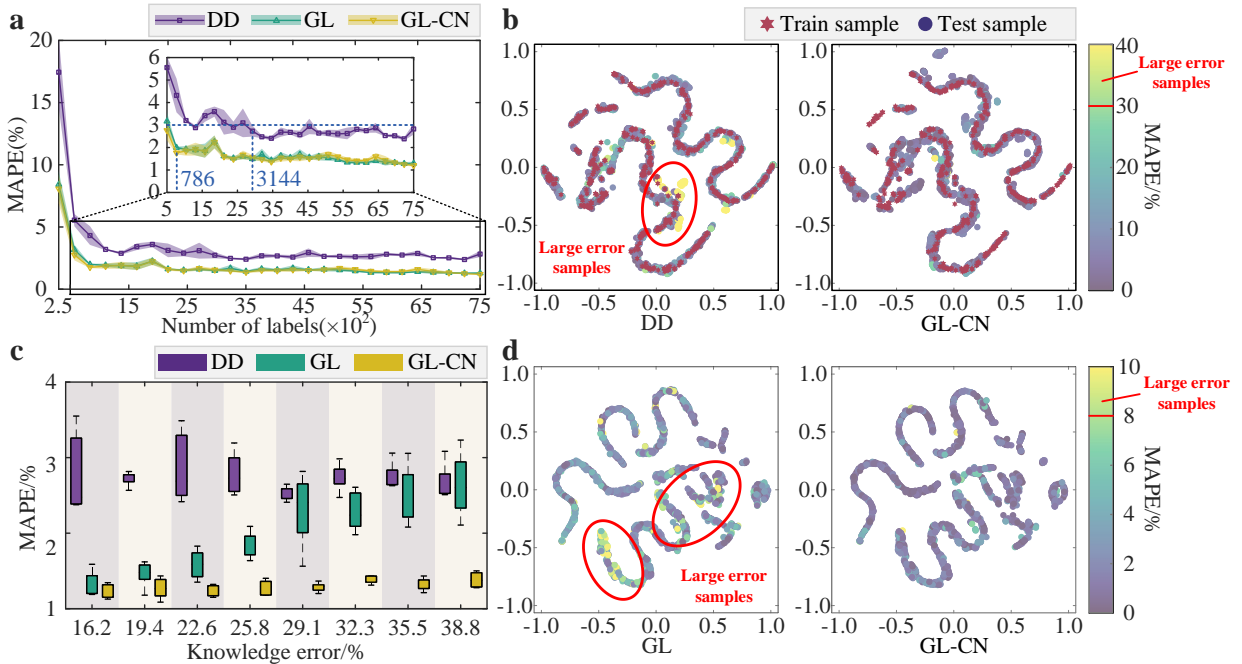


Fig. 4: Model adaptation performance across training set sizes and knowledge accuracy levels, comparing DD, GL, and our GL-CN method.

a MAPE as function of training set size (262-7,336 samples) for all benchmark methods. Inset: zoomed view (500-7,500 samples; MAPE 0-6%). **b** t-SNE visualization of feature distributions (262 samples) comparing DD (left) and GL-CN (right). Training samples (red hexagram) and test samples (gradient circles) are color-coded by predicted MAPE values. **c** MAPE as function of physics-guided knowledge parameter error for all benchmark methods. Increasing parameter errors induce corresponding prediction error growth in KD method. This figure reflect the sensitivity of the benchmark methods to knowledge accuracy. **d** t-SNE feature distributions at 35% parameter error (38.8% knowledge error), comparing GL (left) and GL-CN (right). Test samples (gradient circles) are colored by predicted MAPE values.

While data-knowledge fusion combines the strengths of both approaches, the model's accuracy consequently depends on both dataset size and knowledge precision. These dual dependencies are particularly critical for FSA in power system applications. First, real-world power disturbance events are too scarce to obtain adequate training data, necessitating simulation supplements. However, in large-scale systems, each time-domain simulation requires ~ 40 seconds, making 10,000-sample dataset generation prohibitively time-consuming (~ 5 days). Second, incomplete parameter statistics of actual power systems introduces significant knowledge inaccuracies that substantially degrade model performance. In summary, systematic evaluation of the data-knowledge fusion method's adaptability to varying training set sizes and knowledge precision thresholds is essential to establish its minimum requirements.

The first experiment evaluates model performance across varying training set sizes. Training set sizes ranged from 262 to 7,336 samples, evaluated at 262-sample intervals with five repetitions per condition to ensure statistical reliability. Fig.4a shows the dependence of MAPE on training set size for all three methods: DD, GL, and GL-CN. All models show improvement in accuracy with increasing training samples until reaching a plateau. The GL and GL-CN methods demonstrate nearly identical MAPE values across all dataset sizes, consistently outperforming DD. This performance parity suggests that physics-guided knowledge integration in GL-based methods compensates for data scarcity. With only 262 training samples, the DD method yields a MAPE of $17.44 \pm 2.08\%$, compared to $8.41 \pm 0.84\%$ for our GL-CN approach - a 52% error reduction through physics-guided knowledge integration. To achieve the target MAPE ($< 3\%$), our GL-CN method requires only 786 training samples - a 75% reduction compared to DD's 3,144-sample requirement. Fig.4b compares t-SNE visualizations of feature spaces learned by DD (left) and our GL-CN method (right) using only 262 labeled samples (Supplementary Information). Training samples are marked by red hexagrams, while test samples appear as gradient circles with color intensity scaling from dark (0% MAPE) to light (40% MAPE). The DD method shows precise predictions (MAPE $< 10\%$) in training-covered regions but suffers catastrophic errors (MAPE $> 20\%$) in uncovered areas, revealing its limited generalization capacity. In contrast, our GL-CN method maintains consistent performance (MAPE $< 20\%$) across all test conditions, demonstrating physics-guided knowledge fusion enhances generalization and reduces data requirements.

The second experiment evaluates model robustness to varying knowledge accuracy levels. We systematically varied knowledge accuracy (16.2-38.8% error) by adjusting T_R parameter errors in the physical-guided knowledge from 0% to 35%, which affect f_{nadir} and t_{nadir} . Of this total error, 16.2% stems from model simplification during aggregation, while 16.2% to 38.8% arises from measurement inaccuracies in aggregation parameters, which is detailed in the Supplementary Information. Parameter errors were tested at 5% increments, with five independent training repetitions per condition to ensure statistical reliability. Fig.4c displays the correlation between MAPE and knowledge accuracy for all three

methods (DD, GL, and GL-CN). Three distinct patterns emerge: (1) DD maintains constant 2.85% MAPE regardless of knowledge accuracy; (2) GL performance degrades from 1.59% to 2.91% MAPE as knowledge errors increase; while (3) our GL-CN method demonstrates consistent robustness (1.42% MAPE) across accuracy variations. This robustness stems from the mutual constraints imposed by physics-constrained knowledge integration - the constrained network detects and corrects inaccuracies affecting individual outputs, thereby maintaining overall model fidelity despite localized knowledge errors. Fig.4d compares GL and GL-CN feature spaces under high parameter error (35%, 38.8% knowledge error) using t-SNE. Color gradient (dark to light: 0-10% MAPE) reveals GL-CN's superior robustness: while 15.7% of GL samples exceed 8% MAPE, all GL-CN predictions remain below 8%, with 86.3% achieving $<3\%$ error. This experiment confirms that the constrained network's physics-based architecture enhances model robustness to knowledge inaccuracies, maintaining reliable performance even with 38.8% knowledge error.

2.5 Generalization performance evaluation of the data-knowledge fusion framework

The operational conditions of power systems with high renewable energy penetration are inherently complex and variable. This is particularly evident in the Yunnan Power Grid, where seasonal hydropower availability leads to significant fluctuations in system characteristics. Moreover, as the rate of renewable energy penetration continues to rise, it is highly likely that the testing operational conditions are not covered in the model's training data. Consequently, it is necessary to experimentally validate the generalization capability of the proposed data-knowledge fusion method under unseen scenarios. Using the three benchmark models (KD, DD, and GL-CN) trained in Section 3, we evaluated the data-knowledge fusion method on a generalization test set comprising 17 untrained operational conditions (2,227 samples at 60% renewable energy penetration). This assessment tests the methods' ability to handle increasing renewable penetration levels.

Fig.5a presents the prediction error distributions for frequency metrics across all three methods. The KD method demonstrates strong generalization capability, as it is derived from first principles and independent of training data. Provided accurate assessment of current H and R parameters, it maintains consistent prediction accuracy across varying renewable penetration levels (40-55% to 60%). However, this method exhibits significant systematic error, with only 11.36% of test samples achieving $<5\%$ error while over 40% exceed 20% error - rendering it unreliable for practical implementation. While the DD approach demonstrates reasonable accuracy within the 40-55% penetration range of its training data, its performance degrades significantly at 60% penetration. This heavy dependence on historical data also

limits its adaptability to highly variable power system conditions. The proposed GL-CN method effectively combines the advantages of both approaches, demonstrating superior generalization performance at 60% renewable penetration. While some accuracy degradation occurs, its physics-informed framework maintains significantly better performance than purely KD or DD methods.

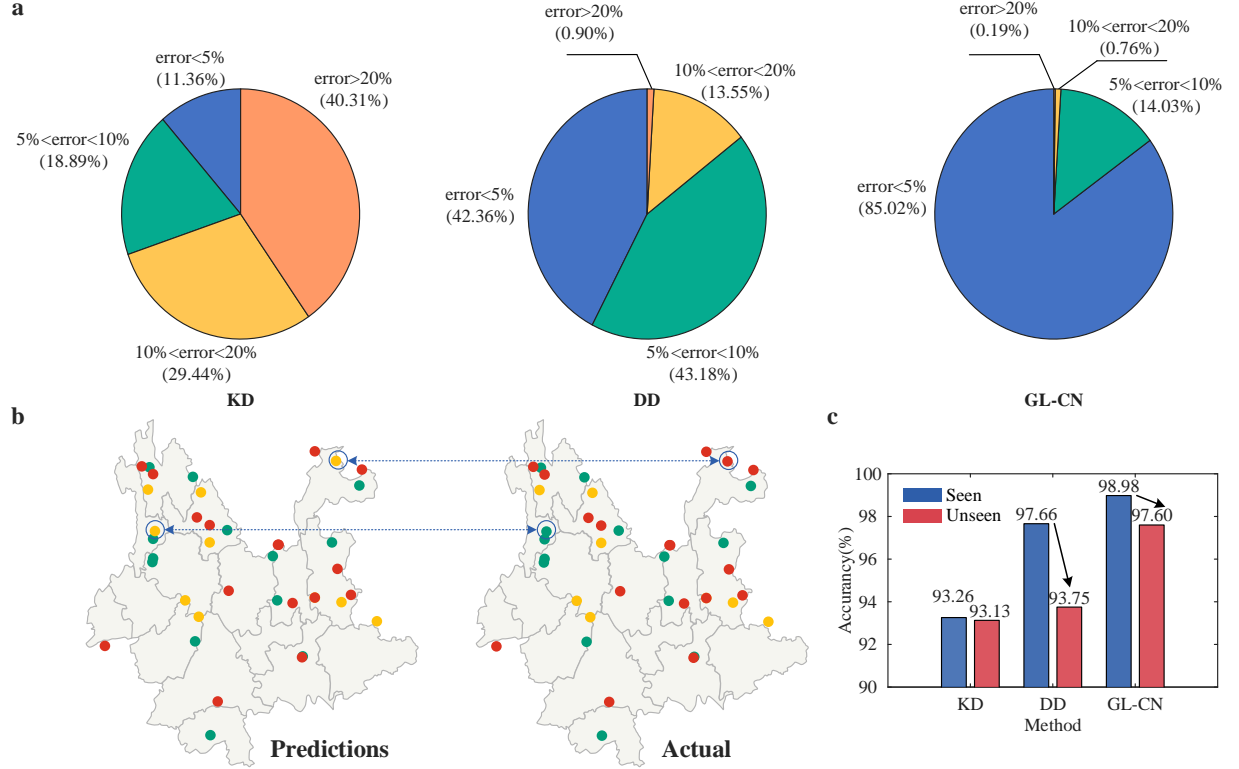


Fig. 5: Generalization performance of the GL-CN framework under 60% renewable energy penetration, benchmarked against KD and DD methods.

a Prediction error distribution across methods: KD (left), DD (center), and GL-CN (right). Errors are categorized into four ranges (<5%, 5–10%, 10–20%, >20%). **b** FSA results using the GL-CN method and the actual data. Data point locations indicate anticipate fault locations, with colors denoting system states: green (secure), yellow (warning), and red (insecure). **c** Frequency security judgment accuracy across the three methods (KD, DD, GL-CN).

Fig.5b presents the FSA results of the GL-CN method under 60% renewable penetration conditions. Corresponding results for the benchmark methods (KD and DD) and reference time-domain simulations are provided in the Supplementary Information. The GL-CN method maintains strong agreement with time-domain simulation benchmarks, demonstrating its robustness for power systems with variable operational conditions. Fig.5c compares the FSA accuracy of all three methods under 60% renewable penetration conditions. Compared to the results in Section 2.3, the KD method maintains 93% accuracy,

while the DD method shows a significant decline to 93.75%. In contrast, the GL-CN method achieves 97.60% accuracy, demonstrating its readiness for practical implementation.

2.6 Comparison with existing methods

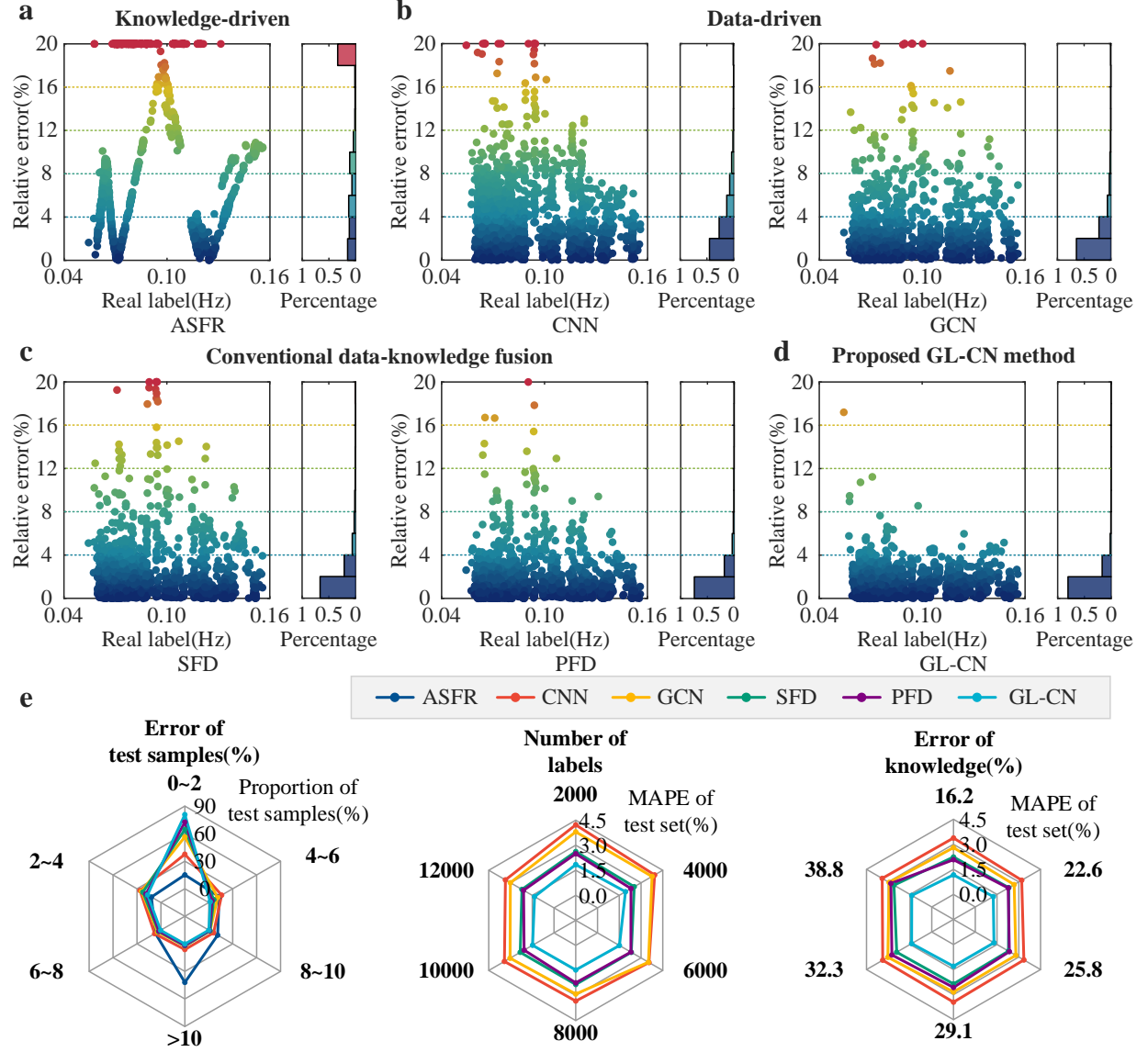


Fig. 6: Comparative performance of KD, DD, and data-knowledge fusion methods in FSA.

a Error distribution of KD methods, including the ASFR model. The scatter plot displays the relationship between predicted and actual frequency security metrics, with relative error indicated by point coloration. The histogram quantifies the sample distribution across error intervals, with bar heights representing the percentage in each bin. **b**

Error distribution of DD methods, including both CNN and GCN architectures. **c** Error distribution of conventional data-knowledge fusion methods, including both SFD and PFD approaches. **d** Error distribution of the GL-CN data-knowledge fusion method. **e** Comparative performance analysis of all six methods, evaluating: 1) error distribution (left), 2) training data volume adaptability (center), and 3) knowledge accuracy robustness (right).

The performance of the proposed data-knowledge fusion method is compared against other three established FSA benchmarks: (1) KD (including ASFR model), (2) DD (including CNN and GCN models), and (3) conventional data-knowledge fusion (including SFD and PFD models), as shown in Fig. 6. Fig. 6a-d presents the error distributions for all four method classes. The high-accuracy samples (<2% error) demonstrate significant performance differences: KD (ASFR: 15.00%), DD (CNN: 37.60%; GCN: 56.45%), conventional data-knowledge fusion (SFD: 64.57%; PFD: 72.59%), and our GL-CN framework (80.71%). The GL-CN framework achieves a maximum error of only 16%, representing 36% and 27.3% reductions compared to SFD (25%) and PFD (22%) respectively, demonstrating significantly enhanced reliability. Fig. 6e demonstrates that the GL-CN method outperforms existing approaches across three critical metrics: (1) error distribution, (2) data volume adaptability, and (3) knowledge accuracy robustness. This superior performance, stemming from the deep integration of fundamental power system principles with DD modeling, confirms GL-CN's strong suitability for real-world large-scale grid applications.

Discussion

Existing FSA methods depend largely on DD models, which limits their robustness and generalization. Consequently, these methods are often inadequate for real-world power systems characterized by complex and diverse operational conditions. In this work, we introduce a framework that integrates power system domain knowledge into both the architecture and training process of deep learning models, establishing a deep data-knowledge fusion paradigm for FSA. This framework categorized domain knowledge into two types — physics-guided and physics-constrained knowledge — and developed a fusion algorithm to enable their deep integration with deep learning models. During pre-training, the incorporation of physics-guided knowledge enabled the model to learn generalized power system frequency response mechanisms, enhancing its performance across diverse scenarios and reducing its reliance on extensive training data. During the prediction phase, a constrained network, trained based on physics-constrained knowledge, corrected the outputs to ensure their physical plausibility.

For the case study, steady-state power flow data, system parameters, and expert-defined anticipated faults were used as inputs to predict post-fault frequency indicators and assess system security. For each power flow condition, the aggregation of predictions across all anticipated faults identified potential risks, offering a reliable basis for proactive system defense. The study utilized 12,707 samples generated from a

model of the Yunnan Provincial Grid in China. Of these, 10,480 samples were allocated for model training and testing under normal conditions, and the remaining 2,227 were reserved for assessing generalization. We first evaluated the model's accuracy: under conventional conditions, the proposed framework achieved an average error of 1.26%, representing a 49.2% reduction compared to the DD method. It also attained 98.98% accuracy in FSA, an improvement of 1.32% over the DD method. Furthermore, robustness was assessed: in data-scarce scenarios, the proposed framework maintains under 3% average error using only 786 samples—a 75% reduction relative to the DD methods. Under knowledge imprecision, the method retained its performance accuracy even at a 38.8% knowledge error level. Finally, we evaluated the model's generalization: it maintained 97.6% accuracy across untrained scenarios of 60% renewable energy penetration—a 3.85% improvement compared to the DD methods. These results demonstrated the method's robustness and practical applicability for real-world large-scale power systems.

However, two aspects of the proposed framework merit further investigation: (1) Optimization of hyperparameters within the fusion algorithm. This work primarily establishes the model and algorithmic framework, utilizing a Monte Carlo approach for knowledge sample generation in the guided learning phase. And the loss function coefficients for the training of constrained network were empirically determined during . Future work should include the systematic optimization of knowledge sample generation strategies and loss function hyperparameters. (2) Development of a credibility metric to quantify prediction uncertainty and enhance decision trustworthiness. Future work should develop a credibility metric based on physics-constrained knowledge, potentially utilizing the KC loss from the constrained network to quantify prediction reliability. Such a metric would critically enhance operator trust in AI-based predictions.

In summary, this work introduces a novel data-knowledge fusion paradigm that demonstrates robust performance and strong generalization in real-world large-scale power systems. The proposed FSA framework has been deployed in the Yunnan Provincial Power Grid in China, delivering accurate and robust AI-assisted predictions for proactive frequency security defense. The proposed data-knowledge fusion algorithm holds potential for broader adoption across power grid sectors and other interdisciplinary domains. The proposed data-knowledge fusion framework demonstrates significant potential for broader applications in engineering beyond power systems. Many engineering prediction problems exhibit gray-box properties: simplified models can approximate influencing factors but lack precision, or inherent physical constraints govern outcomes, yet AI models may violate them. For such scenarios, the GL-CN algorithm leverages approximate models to generate knowledge samples, enabling the training of high-accuracy, high-generalization models with minimal real-world measurement data. Concurrently, physical

constraints between predicted variables are embedded via constraint networks and KC loss, enabling the AI model to internalize these constraints and improve robustness to knowledge inaccuracies. We hope our proposed data-knowledge fusion framework could offer a promising approach to address complex prediction tasks in fields such as weather forecasting and medical diagnostics.

Methods

4.1 Frequency models after power system faults

The frequency of the power system is governed by the rotational speed of synchronous generators, with its dynamic behavior described by the swing equation (Eq.(1)):

$$\frac{2H_i}{f_N} \frac{d\Delta f_i}{dt} + \frac{D_i}{f_N} \Delta f_i = P_{mi} - P_{ei} \quad (1)$$

where f_N denotes the rated system frequency. f_i denotes the frequency of the i^{th} synchronous generator. Δf_i denotes the frequency deviation ($\Delta f_i = f_i - f_N$). H_i denotes the inertia constant. D_i denotes the damping factor. P_{mi} denotes the mechanical power. P_{ei} denotes the electromagnetic power.

The frequency of the center of inertia (f_{COI}), derived from the frequencies of individual synchronous generators, serves as the key system-wide frequency indicator. It is computed as the inertia-weighted average of all generator frequencies, as shown in Eq.(2):

$$f_{COI} = \frac{\sum_{i=1}^N H_i f_i}{\sum_{i=1}^N H_i} \quad (2)$$

where N denotes the generator count.

Under pre-fault steady-state conditions, total generation matches the demand, maintaining the system frequency at its nominal value (50 Hz). Upon a fault, the system frequency deviates. Primary frequency regulation is activated once the frequency deviation surpasses the predetermined deadband (± 0.05 Hz). Frequency regulation strategies differ between synchronous generators (thermal, hydroelectric) and inverter-based resources (photovoltaic, wind power), as shown in Eqs.(3)-(4):

$$P_{Ti} = \frac{K_{mi}(1 + F_{Hi}T_{Ri}s)}{R_i(1 + T_{Ri}s)} \quad (3)$$

where P_{Ti} denotes the power of the i^{th} thermal generator. K_{mi} denotes the mechanical power gain factor. R_i denotes the governor speed regulation. F_{Hi} denotes the high-pressure turbine fraction. T_{Ri} denotes the reheat time constant.

$$P_{Hi} = \frac{K_{mi}(1 - T_{Wi}s)}{R_i(1 + 0.5T_{Wi}s)} \quad (4)$$

where P_{Hi} denotes the power of the i^{th} hydroelectric generator. T_{Wi} denotes the water hammer constant.

4.2 Indicators of frequency security assessment

To accurately assess post-fault frequency security, we define three key metrics corresponding to distinct dynamic phases: the initial response, the frequency nadir, and the quasi-steady-state⁴⁰:

- **Maximum Rate of Change of Frequency ($RoCoF_{max}$):** The initial slope extremum of the frequency trajectory, quantifying disturbance severity during the first moments post-contingency.
- **Nadir Characteristics:** Comprising both the temporal occurrence (t_{nadir}) and magnitude extremum of frequency deviation (f_{nadir}). Exceeding permissible f_{nadir} thresholds risks cascading failures through protective device activation.
- **Quasi-Steady-State Frequency (f_{ss}):** The post-transient equilibrium value indicating system restoration capability.

Among these metrics, f_{nadir} presents particular analytical challenges due to its multivariate dependencies, yet remains paramount for transient stability assessment.

4.3 Knowledge-driven part I: physics-guided knowledge

Physics-guided knowledge enable output prediction through analytical approximations. These models offer dual advantages: computationally efficient formulation for direct intelligent model integration and label generation without intensive simulations. Pure DD training induces distributional bias, particularly problematic in imbalanced datasets (e.g., predominant >49.8 Hz vs. rare <49.5 Hz f_{nadir} instances). Physics-informed pretraining encodes universal system laws, substantially mitigating this bias through systematic modeling approximations. Subsequent fine-tuning focuses primarily on error compensation, achieving enhanced accuracy with reduced training data demands.

The physics-guided knowledge (Eq.(5)-(8)) used for frequency stability assessment (FSA) in renewable-dominated power systems derives from the aggregated system frequency response (ASFR)

model²⁹. This framework enables steady-state approximation of four critical frequency metrics through mechanistic equations under step disturbance conditions:

$$RoCoF_{max} = \frac{1}{2H} \Delta P \quad (5)$$

$$t_{nadir} = \frac{1}{\omega_r} \arctan\left(\frac{T_R \omega_r}{T_R \zeta \omega_n - 1}\right) \quad (6)$$

$$f_{nadir} = \frac{\Delta P}{D + 1/R} (1 + b e^{-\zeta \omega_n t_{nadir}}) \quad (7)$$

$$f_{ss} = \frac{1}{D + 1/R} \Delta P \quad (8)$$

Model parameters are computed through secondary relationships (Eqs.(9)-(14)), encompassing:

$$H = H_{syn} + H_{vir} \quad (9)$$

$$\frac{1}{R} = \sum_{i=1}^N \frac{K_{mi}}{R_i} \quad (10)$$

$$\omega_n^2 = \frac{D + 1/R}{2HT_R} \quad (11)$$

$$\zeta = \frac{DT_R + 2H + F_H T_R / R}{2(D + 1/R)} \omega_n \quad (12)$$

$$\omega_r = \omega_n \sqrt{1 - \zeta^2} \quad (13)$$

$$b = \sqrt{1 - 2\zeta \omega_n T_R + \omega_n^2 T_R^2} \quad (14)$$

where ΔP denotes active power deficit. H the system inertia, including synchronized inertia H_{syn} provided by the synchronous generators and virtual inertia H_{vir} provided by the virtual inertia control of the renewable energy generators. D the damping factor. R the aggregated governor regulation coefficient. R_i the regulation coefficient of the i^{th} generator. K_{mi} the mechanical power gain factor. T_R the turbine time constant. F_H the turbine fraction.

All parameters are obtainable through steady-state monitoring or standard operational assessments. While providing computationally efficient predictions, this formulation omits four critical transient dynamics:

- **Governor nonlinearities:** Governor deadbands and saturation limits are excluded, introducing nonlinear effects during large power deficits.
- **Time-varying virtual inertia:** Renewable-based virtual inertia exhibits temporal variability⁴¹, unaccounted for in constant H_{vir} formulations.
- **Load-frequency coupling:** Frequency-dependent load modulation mechanisms are omitted, eliminating crucial feedback interactions.
- **Reactive power effects:** Q-V dynamics during generation/load shedding remain unmodeled, despite their secondary frequency coupling.

These simplifications necessitate treating ASFR-derived metrics as first-order approximations for initializing DD models rather than precise predictors. The equations (Eqs.(5)-(8)) retain utility as physics-informed priors that: 1) establish baseline system behavior, 2) reduce training data requirements through domain knowledge embedding, and 3) mitigate overfitting risks in neural networks. However, their predictive accuracy remains fundamentally constrained by the aforementioned unmodeled dynamics, requiring hybrid data-knowledge approaches for operational deployment.

4.4 Knowledge-driven part II: physics-constrained knowledge

Domain-expertise-derived operational constraints enhance intelligent model performance by delimiting solution spaces and enforcing physical plausibility. In power system frequency dynamics, temporal-physical constraints are imposed across distinct post-contingency phases:

The first constraint originate from two fundamental mechanisms:

- **Power distribution phase:** At the instant after the disturbance ($t=0^+$), power deficit is distributed to the individual generators according to the synchronized power coefficients.
- **Inertial response phase:** At the beginning of the disturbance ($t=0-500\text{ms}$), the power deficit is gradually shifted to be distributed according to the inertia.

$$\Delta P_{0,i} \approx 2H_i RoCoF_{max,i} \quad (15)$$

$$\Delta P_{0,syn} = 2H_{syn} RoCoF_{max} \quad (16)$$

where $\Delta P_{0,i}$ denotes initial power deficit allocation for the i^{th} synchronous generator (inertia H_i). $\Delta P_{0,\text{syn}}$ the cumulative synchronous generation deficit (system inertia H_{syn}). Eq.(16) constitutes the aggregated form of individual generator constraints in Eq.(15).

Implementation requires temporal alignment between $RoCoF_{\text{max}}$ measurement windows and $P_{0,\text{syn}}$ measurement point. For improved accuracy, $P_{0,\text{syn}}$ measurements should be synchronized with the midpoints of the time window rather than the instant of disturbance.

The second constraint originate from the fundamental mechanisms:

- **Frequency decline phase:** Parabolic frequency trajectory approximation prior to nadir attainment is analytically demonstrated in 26, yielding the fundamental relationship:

$$f_{\text{nadir}} \approx \frac{1}{2} RoCoF_{\text{max}} t_{\text{nadir}} \quad (17)$$

This analytically links critical stability metrics through geometric proportionality.

The third constraint originate from the fundamental mechanisms:

- **Quasi-steady state phase:** At the end of the disturbance ($t > 120\text{s}$), power deficit allocation transitions to damping-dominated dynamics, governed by composite system parameters:

$$D_{eq,i} = D_i + \frac{K_{mi}}{R_i} \quad (18)$$

$$\Delta P_{\infty,i} = D_{eq,i} f_{ss} \quad (19)$$

$$\Delta P_{\infty,\text{syn}} = D_{eq,\text{syn}} f_{ss} \quad (20)$$

where $D_{eq,i}$ denotes the equivalent damping coefficient for the i^{th} governor-equipped synchronous generator, combining inherent damping D_i and governor regulation K_{mi}/R_i . $\Delta P_{\infty,i}$ denotes steady-state power deficit allocation for the i^{th} generator, with $\Delta P_{\infty,\text{syn}}$ and $D_{eq,\text{syn}}$ aggregating system-wide contributions.

Temporal relationships between post-disturbance frequency metrics are leveraged through physics-informed CN construction. Predictions with direct physical couplings (Eqs.(18)-(20)) are interconnected to form topological constraints. The hybrid loss function is formulated as:

$$\mathcal{L} = \mathcal{L}_{\text{MSE}} + \mathcal{L}_{\text{KC}} = \sum_{i=1}^N (\hat{y}_i - y_i)^2 + \sum_{i=1}^N \sum_{j=1}^M \alpha_j e_{ij}^2 \quad (21)$$

where N denotes batchsize. M the constraint quantity. y_i and \hat{y}_i the real and predicted frequency indicators. e_{ij} the j^{th} constraint violation for sample i and α_j the compliance weighting coefficients.

Traditional MSE loss (\mathcal{L}_{MSE}) is combined with knowledge-constraint loss (\mathcal{L}_{KC}) to simultaneously optimize prediction accuracy and physical plausibility.

4.5 Data-driven part: graph convolutional network

Graph Convolutional Networks (GCNs) were developed to address conventional CNNs' inability to incorporate network topology - a critical limitation for power systems where nodal features are predominantly influenced by neighboring nodes. The adjacency matrix (Eq.(22)), which enables this topological modeling through its structural representation of node connectivity, constitutes a fundamental distinction from CNN architectures. For a system with n nodes, the adjacency matrix $A \in \mathbb{R}^{n \times n}$ contains elements a_{ij} defined in Eq.(23):

$$A = \begin{bmatrix} a_{11} & a_{12} & \cdots & a_{1n} \\ a_{21} & a_{22} & \cdots & a_{2n} \\ \vdots & \vdots & \ddots & \vdots \\ a_{n1} & a_{n2} & \cdots & a_{nn} \end{bmatrix} \quad (22)$$

$$a_{ij} = \begin{cases} 1, & \text{if the } i^{\text{th}} \text{ node is connected the } j^{\text{th}} \text{ node} \\ 0, & \text{if the } i^{\text{th}} \text{ node is not connected with } j^{\text{th}} \text{ node} \end{cases} \quad (23)$$

This work employs Graph Sample and Aggregate (GraphSAGE)⁴² for large-scale graph analysis. The layer-wise feature propagation follows:

$$y_i = \sigma(W_1 x_i + W_2 \text{mean}_{j \in N(i)} x_j) \quad (24)$$

where x_i and y_i denote the layer's input and output features for node i , with $W_1, W_2 \in \mathbb{R}^{d_1 \times d_2}$ as trainable weight matrices. The activation function $\sigma(\cdot)$ introduces non-linearity, while $N(i)$ denotes the neighborhood node set. The $\text{mean}(\cdot)$ operator aggregates neighboring features through element-wise averaging.

4.6 The data-knowledge fusion algorithm: guided learning-knowledge network

We present the GL-KN algorithm, a data-knowledge fusion framework for power system analysis. The methodology comprises four sequential phases:

- **Initialization.** System samples are first annotated with knowledge labels derived from domain-specific illumination knowledge. A randomized subset is subsequently selected for time-domain simulations to obtain ground-truth labels.
- **Guided Learning I: Knowledge-Based Pretraining.** The multilayer perceptron undergoes pre-training to establish correlations between global system data and knowledge labels, exclusively updating network parameters through this knowledge-driven initialization.
- **Guided Learning II: Real-Label Fine-Tuning.** Model parameters are refined using ground-truth labels while incorporating topological-embedded local data to capture spatial disturbance effects. This dual-data integration enhances location-aware prediction capabilities.
- **Knowledge Network Integration.** A hybrid labeling strategy is implemented: real labels for simulated samples and pseudo-labels for others. The network architecture incorporates a KN and KC loss function to enforce physical consistency and ensure the robustness of the prediction.

The trained framework enables real-time frequency stability assessment (FSA) using steady-state operational data. Operators input high-risk disturbance scenarios to obtain immediate frequency response predictions. The system performs case-by-case verification against domain knowledge, routing non-compliant predictions through the KN for corrective refinement. This dual-validation architecture enhances result credibility while maintaining computational efficiency suitable for grid-scale applications.

4.7 Baseline methods

We evaluate four comparative FSA approaches while maintaining equivalent data architectures and hyperparameters to highlight knowledge fusion effects:

- **Knowledge-Driven (KD):** Implements analytical relationships from the ASFR model (Eqs.(5)-(8)), where system inputs are directly computed through first-principle equations.
- **Data-Driven (DD):** Pure machine learning implementations (RF, MLP, CNN, GCN) employing prediction without physical constraints.
- **Serial Fusion-Driven (SFD):** A cascaded architecture where KD approximations are refined through subsequent DD correction layers.
- **Parallel Fusion-Driven (PFD):** A hybrid prediction scheme that strategically allocates well-defined relationships to physics-based computation and complex patterns to machine learning regression.

Data Availability

For more information on data availability, click [here](#). Certain data types must be deposited in an appropriate public structured data depository (details are available [here](#)) and the accession number(s) provided in the manuscript. Full access is required at acceptance. Should full access to data be required for peer review, authors must provide it. *Nature Communications* encourage provision of other source data in unstructured public depositories such as [Dryad](#) or [figshare](#), or as supplementary information. To maximize data reuse, *Nature Communications* encourage publication of detailed descriptions of datasets in [Scientific Data](#).

Code Availability

Research papers using custom computer code will also be asked to fill out a [code and software submission checklist](#) that will be made available to editors and reviewers during manuscript assessment. The aim is to make studies that use such code more reliable by ensuring that all relevant documentation is available and by facilitating testing of software by the reviewers. Further detailed guidance and required documentation at submission and acceptance of the manuscript can be found [here](#).

References

1. Hatziargyriou N, Milanovic J, Rahmann C, et al. Definition and classification of power system stability–revisited & extended[J]. IEEE Transactions on Power Systems, 2020, 36(4): 3271-3281.
2. Wang Y, Wang R, Tanaka K, et al. Accelerating the energy transition towards photovoltaic and wind in China[J]. Nature, 2023, 619(7971): 761-767.
3. Homan S, Mac Dowell N, Brown S. Grid frequency volatility in future low inertia scenarios: Challenges and mitigation options[J]. Applied Energy, 2021, 290: 116723.
4. Saha S, Saleem M I, Roy T K. Impact of high penetration of renewable energy sources on grid frequency behaviour[J]. International Journal of Electrical Power & Energy Systems, 2023, 145: 108701.

5. Bialek J. What does the GB power outage on 9 August 2019 tell us about the current state of decarbonised power systems?[J]. *Energy Policy*, 2020, 146: 111821.
6. Youvan D C. Simulation Iberia: Modeling a Silent Electromagnetic Strike Through the 2025 Iberian Blackout[J]. 2025.
7. Xu L, Lin N, Poor H V, et al. Quantifying cascading power outages during climate extremes considering renewable energy integration[J]. *Nature communications*, 2025, 16(1): 2582.
8. Sundar S, Craig M T, Payne A E, et al. Meteorological drivers of resource adequacy failures in current and high renewable Western US power systems[J]. *Nature Communications*, 2023, 14(1): 6379.
9. Knap V, Chaudhary S K, Stroe D I, et al. Sizing of an energy storage system for grid inertial response and primary frequency reserve[J]. *IEEE Transactions on power systems*, 2015, 31(5): 3447-3456.
10. Linaro D, Bizzarri F, Del Giudice D, et al. Continuous estimation of power system inertia using convolutional neural networks[J]. *Nature Communications*, 2023, 14(1): 4440.
11. Tang Z, Yang Y, Blaabjerg F. Power electronics: The enabling technology for renewable energy integration[J]. *CSEE Journal of Power and Energy Systems*, 2021, 8(1): 39-52.
12. Cheng Y, Azizipanah-Abarghooee R, Azizi S, et al. Smart frequency control in low inertia energy systems based on frequency response techniques: A review[J]. *Applied Energy*, 2020, 279: 115798.
13. Chen W, Zheng T, Nian H, et al. Multi-objective adaptive inertia and droop control method of wind turbine generators[J]. *IEEE Transactions on Industry Applications*, 2023, 59(6): 7789-7799.
14. Pawar B, Batzelis E I, Chakrabarti S, et al. Grid-forming control for solar PV systems with power reserves[J]. *IEEE Transactions on Sustainable Energy*, 2021, 12(4): 1947-1959.

15. Sun M, Sun Y, Chen L, et al. Novel temporary frequency support control strategy of wind turbine generator considering coordination with synchronous generator[J]. IEEE Transactions on Sustainable Energy, 2022, 13(2): 1011-1020.
16. Zhang Y, Zhu H, Wang X. Prediction for the maximum frequency deviation of post-disturbance based on the deep belief network[C]//2019 IEEE Innovative Smart Grid Technologies-Asia (ISGT Asia). IEEE, 2019: 683-688.
17. Xu Y, Dai Y, Dong Z Y, et al. Extreme learning machine-based predictor for real-time frequency stability assessment of electric power systems[J]. Neural Computing and Applications, 2013, 22: 501-508.
18. Ren J, Chen J, Shi D, et al. Online multi-fault power system dynamic security assessment driven by hybrid information of anticipated faults and pre-fault power flow[J]. International Journal of Electrical Power & Energy Systems, 2022, 136: 107651.
19. Sattar F, Ghosh S, Isbeih Y J, et al. A predictive tool for power system operators to ensure frequency stability for power grids with renewable energy integration[J]. Applied Energy, 2024, 353: 122226.
20. Ma C, Wang L, Gai C, et al. Frequency security assessment for receiving-end system based on deep learning method[C]//2020 IEEE/IAS Industrial and Commercial Power System Asia (I&CPS Asia). IEEE, 2020: 831-836.
21. Zhang T, Xin L, Wang S, et al. A novel approach of energy and reserve scheduling for hybrid power systems: Frequency security constraints[J]. Applied Energy, 2024, 361: 122926.
22. Jiang B, Guo C, Chen Z. Frequency constrained unit commitment considering reserve provision of wind power[J]. Applied Energy, 2024, 361: 122898.
23. Wang Q, Yao L, Li W, et al. A frequency control method based on a coordinated active and reactive power optimization adjustment for weak HVDC sending-end power grid[C]//2020 IEEE 4th Conference on Energy Internet and Energy System Integration (EI2). IEEE, 2020: 3275-3281.

24. Zhao Y, Xie K, Shao C, et al. Integrated assessment of the reliability and frequency deviation risks in power systems considering the frequency regulation of DFIG-based wind turbines[J]. IEEE Transactions on Sustainable Energy, 2023, 14(4): 2308-2326.
25. Zhang G, Ren J, Zeng Y, et al. Security assessment method for inertia and frequency stability of high proportional renewable energy system[J]. International Journal of Electrical Power & Energy Systems, 2023, 153: 109309.
26. Liu L, Li W, Ba Y, et al. An analytical model for frequency nadir prediction following a major disturbance[J]. IEEE Transactions on Power Systems, 2020, 35(4): 2527-2536.
27. Zhang Z, Du E, Teng F, et al. Modeling frequency dynamics in unit commitment with a high share of renewable energy[J]. IEEE Transactions on Power Systems, 2020, 35(6): 4383-4395.
28. Anderson P M, Mirheydar M. A low-order system frequency response model[J]. IEEE transactions on power systems, 2002, 5(3): 720-729.
29. Shi Q, Li F, Cui H. Analytical method to aggregate multi-machine SFR model with applications in power system dynamic studies[J]. IEEE Transactions on Power Systems, 2018, 33(6): 6355-6367.
30. Ren Y, Wan C, Xiao R, et al. An Aggregated Frequency Response Model for Power Systems with Renewables[C]//2023 IEEE/IAS Industrial and Commercial Power System Asia (I&CPS Asia). IEEE, 2023: 422-428.
31. Wang C, Li B, Liu C, et al. Convolutional neural network-based power system frequency security assessment[J]. IET Energy Systems Integration, 2021, 3(3): 250-262.
32. Huang T, Guo Q, Sun H, et al. A deep spatial-temporal data-driven approach considering microclimates for power system security assessment[J]. Applied energy, 2019, 237: 36-48.

33. Zhang Y, Shi X, Zhang H, et al. Review on deep learning applications in frequency analysis and control of modern power system[J]. International Journal of Electrical Power & Energy Systems, 2022, 136: 107744.
34. Shi Z, Yao W, Li Z, et al. Artificial intelligence techniques for stability analysis and control in smart grids: Methodologies, applications, challenges and future directions[J]. Applied Energy, 2020, 278: 115733.
35. Ibrahim M S, Dong W, Yang Q. Machine learning driven smart electric power systems: Current trends and new perspectives[J]. Applied Energy, 2020, 272: 115237.
36. Machlev R, Heistrene L, Perl M, et al. Explainable Artificial Intelligence (XAI) techniques for energy and power systems: Review, challenges and opportunities[J]. Energy and AI, 2022, 9: 100169.
37. Wang Q, Li F, Tang Y, et al. Integrating model-driven and data-driven methods for power system frequency stability assessment and control[J]. IEEE Transactions on Power Systems, 2019, 34(6): 4557-4568.
38. Lin J, Zhang Y, Liu J, et al. A physical-data combined power grid dynamic frequency prediction methodology based on adaptive neuro-fuzzy inference system[C]//2018 International Conference on Power System Technology (POWERCON). IEEE, 2018: 4390-4397.
39. Yu R, Wang R. Learning dynamical systems from data: An introduction to physics-guided deep learning[J]. Proceedings of the National Academy of Sciences, 2024, 121(27): e2311808121.
40. Cheng Y, Azizpanah-Abarghoee R, Azizi S, et al. Smart frequency control in low inertia energy systems based on frequency response techniques: A review[J]. Applied Energy, 2020, 279: 115798.
41. Li Y, Yao W, Zhao Y, et al. Real-time estimation of time-varying inertia for non-synchronous devices using streaming dynamic mode decomposition[J]. International Journal of Electrical Power & Energy Systems, 2024, 157: 109847.

42. Hamilton W, Ying Z, Leskovec J. Inductive representation learning on large graphs[J]. Advances in neural information processing systems, 2017, 30.

Acknowledgements

Keep acknowledgements brief and do not include thanks to anonymous referees or editors, or effusive comments. Grant or contribution numbers may be acknowledged.

Ethics declarations

Competing interests

Submission of a competing interests statement is required for all content of the journal.